Available online at www.sciencedirect.com

ScienceDirect

Ceramics International 42 (2016) 3077–3087

CERAMICS INTERNATIONAL

www.elsevier.com/locate/ceramint

# Shape-controlled agglomeration of $TiO_2$ nanoparticles. New insights on polycrystallinity vs. single crystals in photocatalysis

K. Vajda[a,1], K. Saszet[b,1], E.Zs. Kedves[b,1], Zs. Kása[a], V. Danciu[b], L. Baia[c,d], K. Magyari[c,d], K. Hernádi[a,e], G. Kovács[b,c,*], Zs. Pap[a,b,c,*]

[a]Research Group of Environmental Chemistry, Institute of Chemistry, University of Szeged, Tisza Lajos krt. 103, HU-6720 Szeged, Hungary
[b]Faculty of Chemistry and Chemical Engineering, Babeş-Bolyai University, Arany János 11, RO-400028 Cluj-Napoca, Romania
[c]Faculty of Physics, Babeş-Bolyai University, M. Kogălniceanu 1, RO-400084 Cluj-Napoca, Romania
[d]Institute for Interdisciplinary Research on Bio-Nano-Sciences, Babeş-Bolyai University, Treboniu Laurian 42, RO-400271 Cluj-Napoca, Romania
[e]Department of Applied and Environmental Chemistry, University of Szeged, Rerrich Béla tér 1, 6720 Szeged, Hungary

Received 2 July 2015; received in revised form 3 July 2015; accepted 19 October 2015
Available online 24 October 2015

**Abstract**

The photocatalytic activity of $TiO_2$ photocatalysts depends mainly on its crystal phase composition, primary particle size and specific surface area. Shape manipulation is an interesting way to increase the photocatalytic efficiency. The shape-tuning can be carried out at different levels, both at single crystal and polycrystalline agglomeration levels. The aim of our present study was to compare the structural and photocatalytic performances of two type/level of crystal organization of $TiO_2$, namely single crystal shaping vs. polycrystalline/shape tailored agglomeration. The morphological analysis was achieved by XRD, SEM, TEM, Raman spectroscopy, DRS. The photocatalytic performance of the materials was evaluated by the degradation of a model pollutant (phenol). It was found, that both shape manipulating approaches bear the necessary potential which can be exploited in future development of efficient photocatalysts' synthesis procedures.


*Keywords:* Titania; Crystal growth; Polycrystalline system; Single crystals; Surface normalized photocatalytic activity

## 1. Introduction

Nowadays several papers are focused on heterogeneous photocatalysis due to the increase of environmental problems, including water and air pollution. It is known that the photoactivated semiconductor oxides are able to decompose various kinds of organic pollutants from water (dyes, phenol and phenolic compounds) and also from air (e.g. VOCs) which are toxic and non-biodegradable under normal conditions [1–3].

One of the widely studied, promising semiconductor photocatalyst is titanium-dioxide ($TiO_2$) [4]. The reasons why this material is so popular are: the biological and chemical inertness, cost effectiveness and long-term stability against photo- and chemical corrosion, and its high quantum yield. Additionally, there are many other possible applications of the nano-sized $TiO_2$ such as dye-sensitized solar cells (DSSC), chemical sensors [5,6] and photocatalytic $H_2$ production [7,8]. Furthermore, high number of studies revealed that a large spectrum of harmful organic contaminants can be degraded by $TiO_2$ nanoparticles [9–13]. The photocatalytic performance depends on many structural/morphological and optical parameters of the chosen semiconductor, shape, size, crystallinity, the crystal structure (crystal phases) and the reactive crystal facets. In the case of titania three crystal phases are well-known: rutile, anatase and brookite [14]. Anatase usually possess higher photocatalytic activity than other crystal phases thanks to its better charge ($e^-/h^+$ pairs) separation efficiency and higher electron mobility [15,16]. The photocatalytic performance can be influenced by modifying other parameters, such as crystallite size, surface area, etc. Furthermore, the

*Corresponding authors at: Faculty of Chemistry and Chemical Engineering, Babeş-Bolyai University, Arany János 11, RO-400028 Cluj-Napoca, Romania.
*E-mail addresses:* gkovacs@chem.ubbcluj.ro (G. Kovács), pap.zsolt@phys.ubbcluj.ro (Zs. Pap).
[1]First authors.

http://dx.doi.org/10.1016/j.ceramint.2015.10.095
0272-8842/

tuning of the structural properties of $TiO_2$ can be easily carried out applying simple crystallization methods, such as the calcination [17,18].

Unfortunately the bare $TiO_2$ has lower activity under visible light, thus it is necessary to include them in composite materials with other semiconductors or/and doping with metals [19]. Useful semiconductor oxides for this purpose can be $SnO_2$, $SiO_2$, $WO_3$ [20], etc. Another possible solution is the deposition of noble metal nanoparticles (Au, Pt, etc.) on the titania surface [21].

Recently researchers combined $TiO_2$ with different type of carbons and nanocarbons to increase the lifetime of the charge carriers: activated carbon, carbon nanotubes (CNTs) and graphene [22–24]. Carbon–$TiO_2$ composites are so-called "rising star"-type of materials applied successfully in the degradation of various pollutants [25], while some of them were proven to be also biocompatible [26].

As it is known, the photocatalytic efficiency in the case of $TiO_2$ is influenced by the particle size, crystal phase, the main reactive crystal facets and the partner materials' nature in the case of composite materials (noble metals, semiconductors or carbon materials) [27–30]. The (001) crystal facets have higher photocatalytic activity (oxidative power) compared to the (100) or (101) crystallographic surfaces, especially at nanometer scale [31–34]. The (001) planes can be grown in the presence of $F^-$, which are very efficient species in the shape tailoring of $TiO_2$ nanoparticles [35–37]. There are some papers regarding the improvement of rutile's photocatalytic activity by the formation of (111) facet dominated pyramid-shaped nanoparticles [38]. "Shape-reforming" is indeed a powerful tool for the increase of the photocatalytic efficiency as shown above. However, shape manipulation can be executed at different levels. The "classical way" is the morphology control at crystallite level (single crystals), while a more difficult challenging modality of shape tuning is the hierarchical shape build-up.

One good example is the $TiO_2$ hierarchical nanorod-spheres which were found to be quite efficient in photocatalytic applications, due to their enhanced light absorption capability, enlarged specific surface area and enhanced charge transfer rate of photogenerated electrons [39]. These $TiO_2$ crystals can be built also in nano- and micro particle size range possessing two morphology types at two levels: three dimensional (3D) $TiO_2$ nanostructures made up of one dimensional (1D) $TiO_2$ nanorods. The shape-controlled synthesis of the above mentioned materials were carried out applying several synthesis routes, such as: hydrothermal crystallization [40–43], anodic oxidation [44,45] and template assisted synthesis [46–48].

As it was presented above, two morphology control strategies can be found in the literature: one of them focuses on the individual shape-tailoring of single crystals, while the other one is centered on the importance of the agglomeration of the single crystals in secondary geometries. Consequently, it would be crucial to see the influence of the different shape tailoring approaches (hierarchical vs. single crystal) on the photocatalytic activity of $TiO_2$, while keeping in focus the different structural peculiarities of the specific titania morphology.

## 2. Experimental section[2]

### 2.1. Materials

Titanium tetrachloride ($TiCl_4$; 99.9%, Aldrich); sodium dodecyl sulfate (SDS, $CH_3(CH_2)_{11}OSO_3$ 99% Aldrich), thiourea ($H_2NCSNH_2$; 98%, Aldrich), HCl 37% (Sigma-Aldrich, Germany), HF 40% (Sigma-Aldrich, Germany), 2-propanol (anhydrous, 99.5%; Sigma-Aldrich, Germany), 69% (Reanal NORMAPUR), $Ti(OBu)_4$ 97% (Aldrich, USA), commercially available $TiO_2$ powder (Aeroxide P25, Evonik Industries) and phenol (ReAnal NORMAPUR) were used as received.

### 2.2. Hydrothermal synthesis of the egg-shaped $TiO_2$

SDS (5.3 g) was dissolved in distilled water and mixed with 7 g of thiourea. After complete solubilization, the titanium precursor ($TiCl_4$) was added drop-wise to this aqueous solution under vigorous stirring. During the addition of the precursor caution should be taken on the quick release of HCl as $TiCl_4$ it is extremely sensitive to moisture. This mixture was stirred at 50 °C for 1 h to yield a transparent solution. Into the previous mixture 1 mL of HCl (37%) was added three times in the last 15 minutes (1 mL of HCl/5 min). The final molar ratios applied during the synthesis were: $TiCl_4$: SDS: thiourea: HCl: $H_2O$ = 1:2:10:11:300. The solution was immediately transferred into a sealed, Teflon-coated autoclave and was further heated to 180 °C for 36 h. The obtained white precipitate was washed several times with distilled water until no $H_2S$ was noticed and the organic impurities were completely removed. After this, the product was dried in an oven at 80 °C for 24 h, under air flow. The titania nanocrystallites were calcined at four different temperatures (500, 650, 800 and 1000 °C), at a heating rate of 4 °C $min^{-1}$ for 3 h in a muffle furnace. These samples were coded as follows: ME-X – **m**icro-**e**ggs-X (the value of the calcination temperature).

### 2.3. Hydrothermal synthesis of the single crystal anatase $TiO_2$

In a typical synthesis of the $TiO_2$ microcrystals: 8 mL tetrabutil titanante $Ti(OBu)_4$ was added into 104 mL, HCl solution (5 mol $L^{-1}$), under magnetic stirring for 30 min at room temperature. After that 2.475 mL HF (47%) was added to the mixture. Following a 5 min long vigorous stirring, the resulting solution was transferred into a Teflon-lined stainless steel autoclave. Additionally 40 mL of HCl (5 mol $L^{-1}$) was also added to the autoclave. The device was maintained at 180 °C for 1, 5, and 24 h. Afterwards, the autoclave was cooled down using a continuous water jet for 30 min. The product was washed several times with 2:1 (v/v) mixture of 2-propanol and distilled water. This

[2]Please note that the formation mechanism of the obtained nanomaterials it is not discussed, as the main subject is on the photocatalytic activity of these materials in the frame of the polycrystallinity (crystal geometries formed by crystallization/agglomeration) vs. single crystals (with exposed facets).

purification step was repeated until the pH of the supernatant was above 6. Finally, the samples were dried at 80 °C for 24 h in air. The obtained powders were calcined at 400 °C for 2 h. These samples were coded as follows: MP-X – **m**icro-**p**lates-X (the duration of the hydrothermal treatment)). Sample MP-1H is not discussed in-detail in Section 3 as the yield of the synthesis procedure is very low and the obtained material contains a significant amount of amorphous material (based on preliminary Raman spectroscopy investigations).

### 2.4. Methods and instrumentation

Crystalline phases were determined by X-ray diffractometry (XRD, Shimadzu 6000) using Cu-Kα radiation ($\lambda = 1.5406$ Å) equipped with a graphite monochromator. The crystallites average size was calculated using the Scherrer equation [49].

JASCO-V650 spectrophotometer with an integration sphere (ILV-724) was used for measuring the DRS spectra of the samples (250–800 nm). To obtain the band-gap energy the reflectance data were converted to $F(R)$ values according to the Kubelka–Munk theory. The band gap was obtained from the plot of $[F(R)\ E]^{1/2}$ versus energy of the exciting light ($E$). The possible electron transitions' wavelengths were evaluated by plotting the dR $d\lambda^{-1}$ vs. λ, where R is the reflectance and λ is the wavelength [50].

The FT-Raman spectra were recorded by using a Bruker Equinox 55 spectrometer with an integrated FRA 106 Raman module using an Nd-YAG laser (1064 nm). Raman spectra were recorded with a spectral resolution of 1 $cm^{-1}$.

The microstructure of the samples was analyzed by the field-emission scanning electron microscopy (SEM), FEI Quanta 3D FEG operating at 20 kV. Samples for SEM were attached to a carbon adhesive pad which was fixed to an aluminum stub. Also the samples were examined by transmission electron microscopy (TEM). The TEM micrographs were recorded on a Philips CM 10 instrument operating at 100 kV using coated copper grids. These studies were performed to characterize the particle and size distribution and also to observe the morphology of the particles.

#### 2.4.1. Photocatalytic runs

The reaction conditions for the photocatalytic efficiency experiments were chosen based on our earlier experiences [50]. A photoreactor system with $3 \times 60$ W low pressure fluorescent lamps ($\lambda_{max} \approx 365$ nm) were used to measure the photocatalytic activities. The irradiation distance was 15 cm, while the irradiation time in the case of MEs was 2 h, respectively 3 h for the MPs (due to the low degradation efficiencies). The photocatalyst suspension containing phenol ($C_{0,\ phenol} = 0.5$ mM; $C_{TiO_2} = 1.0$ g/L; $V_{suspension}$ 50 mL) was continuously purged by air in order to maintain the dissolved oxygen concentration during the experiment. The concentration decrease of the chosen organic substrate was followed using an Agilent 1100 series HPLC system (instrumental details can be found consulting reference [23,50]). Based on the initial phenol concentration and the HPLC chromatograms the final phenol concentration and the degradation rates were determined [23]. The surface normalized phenol removal intensities were evaluated using Eq. (1), where $C_0$ is the initial concentration of phenol, while $C_t$ is the concentration at a given time of phenol and $S$ is the specific surface area:

$$C_S\left(\frac{mM\ \textbf{degraded phenol}}{m^2}\right) = \frac{C_0 - C_t}{S} \quad (1)$$

The surface normalized reaction rate was evaluated by fitting an empirical function to the $f(t) = C_S$ data series points.

## 3. Results and discussions

### 3.1. Structure and morphology of egg-shaped $TiO_2$

Fig. 1 shows the X-ray diffraction (XRD) patterns of the as-synthesized and calcined titania nanoparticles, prepared from $TiCl_4$. The hydrothermally crystallized ME sample series contained only the anatase crystal phase which was evidenced from the identified diffraction peaks (JCPDS card no. 00-075-1537). As mentioned in the experimental section, the samples were calcined at different temperatures (500, 650, 800 and 1000 °C) to achieve higher crystallinity grade which can result in higher photocatalytic activity [51]. The characteristic anatase peaks became sharper as higher calcination temperatures were applied, indicating an increase in the crystallites' size. Interestingly, the anatase phase remained stable up to 800 °C, none of these samples showing specific diffraction peaks of rutile (JCPDS card no. 00-075-1748). However, a complete rutilization occurred at 1000 °C (sample ME-1000). Similar high anatase stability were already observed by other research groups [52,53]. The crystallite size values of the hydrothermal synthesized and the calcined titania nanoparticles were calculated by employing Debye-Scherrer equation. The initial and the calcined photocatalysts (500, 650, 800 °C) consisted from 15 (ME) up to 21 nm (ME-800) nanocrystals (Table 1). Increasing the calcination temperature indicates a gradual growth of the crystallite, until the anatase rutile transformation occurs. Based just on the XRD patterns no clear signs have been detected which indicated that these nanocrystals are shape tailored or they are part of a

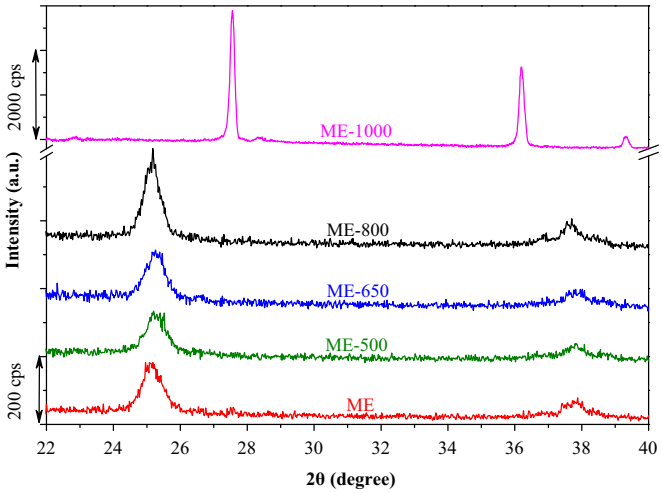


Fig. 1. XRD patterns of the ME sample series.

Table 1
Structural and photocatalytic data of the investigated samples.

| Sample | Crystal phase | Band-gap ($E_g$) (eV) | Particle size [#](nm) [*](μm) | Surface area ($m^2\ g^{-1}$) | Initial degradation rate of phenol ($r_0$) ($mM\ min^{-1}$)·$10^{-3}$ | Surface normalized degradation intensity of phenol ($r_{SNI}$) ($mM\ m^{-2}\ min^{-1}$)·$10^{-4}$ | Degradation yield (%) |
|---|---|---|---|---|---|---|---|
| ME | Anatase | 3.12 | 15.4 | 91.51 | 3.31 | 0.18 | 39.4 |
| ME-500 | Anatase | 3.16 | 17.1 | 82.94 | 1.18 | 0.25 | 46.0 |
| ME-650 | Anatase | 3.20 | 16.8 | 84.43 | 3.24 | 0.28 | 48.8 |
| ME-800 | Anatase | 3.24 | 20.7 | 68.52 | 3.72 | 0.37 | 61.2 |
| ME-1000 | Rutile | 3.00 | ~2[*] | 0.22 | Inactive | – | – |
| MP-5H | Anatase | 3.15 | ~1-2[*] | 0.57 | 0.33 | 5.81 | 11.3 |
| MP-5H C | Anatase | 2.74 | ~1-2[*] | 0.52 | 0.47 | 9.27 | 13.6 |
| MP-24H | Anatase | 2.83 | ~1-2[*] | 0.49 | 0.15 | 6.16 | 12.9 |
| MP-24H C | Anatase | 3.09 | ~1-2[*] | 0.45 | 0.59 | 13.66 | 19.4 |
| P25 | [**] | 3.10 | 40 | 49.1 | 6.71 | 0.41 | 70.2 |

[*]For the size and shape factor distribution please consult Fig. 4.
[**]89 wt% anatase and 11 wt% rutile.

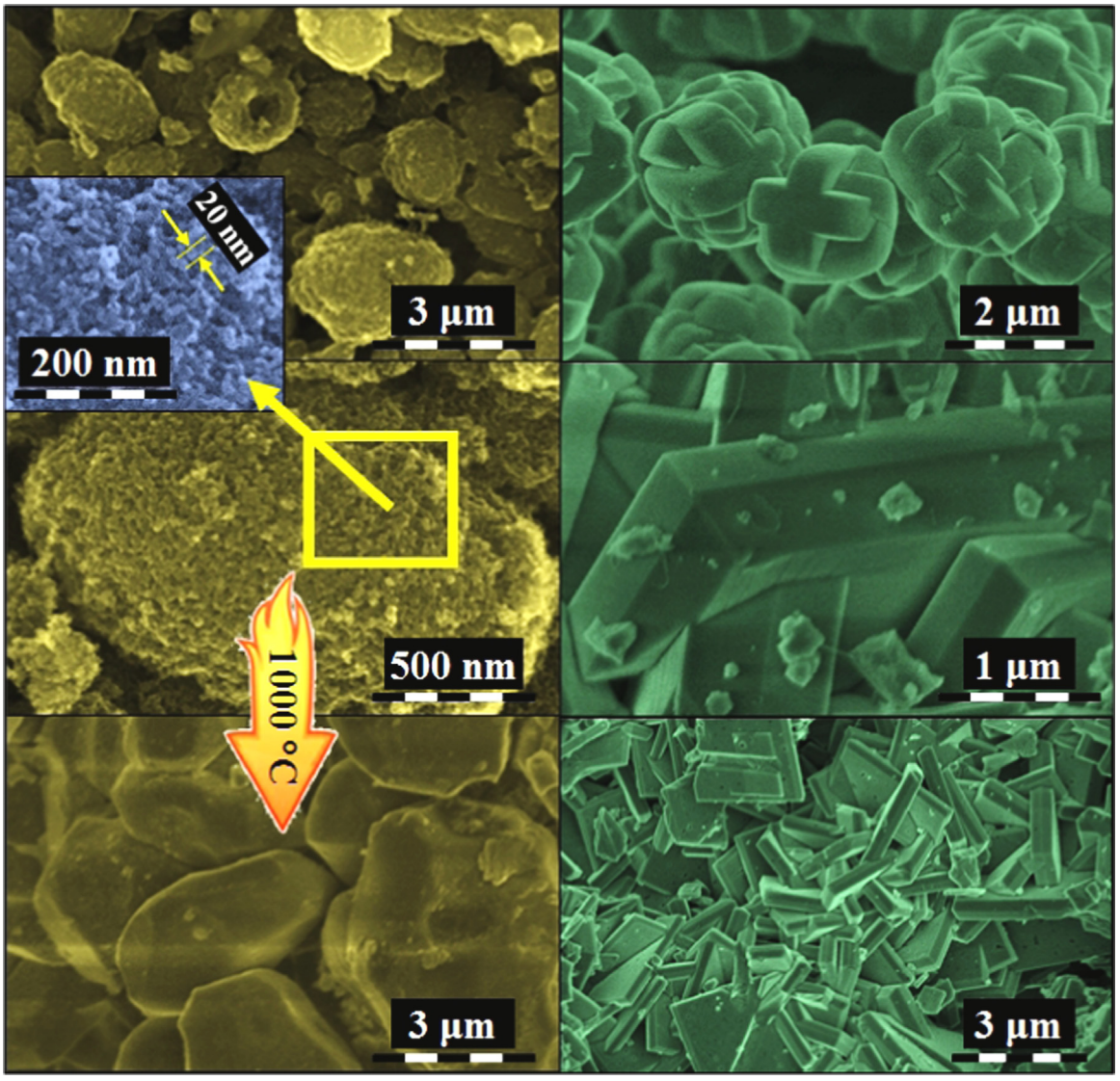


Fig. 2. SEM micrographs of the hydrothermally obtained and calcined ME (yellow) and MP (green) photocatalyst series (the flame arrow indicates the calcination procedure, which in the case of MP was 400, while for ME in this particular case 1000 °C). (For interpretation of the references to color in this figure legend, the reader is referred to the web version of this article.)

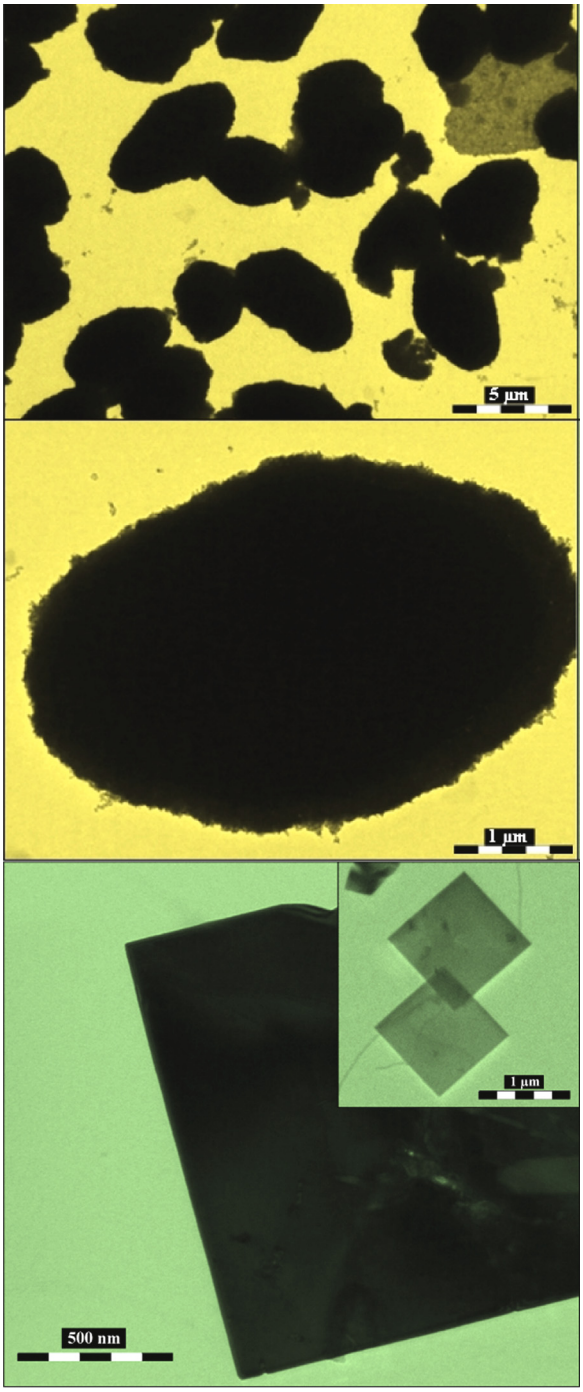


Fig. 3. TEM micrographs of the ME (yellow) and MP (green) sample series. (For interpretation of the references to color in this figure legend, the reader is referred to the web version of this article.)

secondary geometry. To enlighten this aspect electron microscopy images were evaluated.

Typical SEM/TEM images of the ME series are shown in Figs. 2a, b and 3, pointing out the formation of "egg-like" microstructures. The egg shape's occurrence was high (76%), although some randomly agglomerated crystals were also found. They exhibit a relatively high monodispersity: an average width ($D$) of 2.2 µm ($\pm$ 13%) and a length ($L$) 3.3 ($\pm$ 15%) µm. The ratio of $L$ and $D$

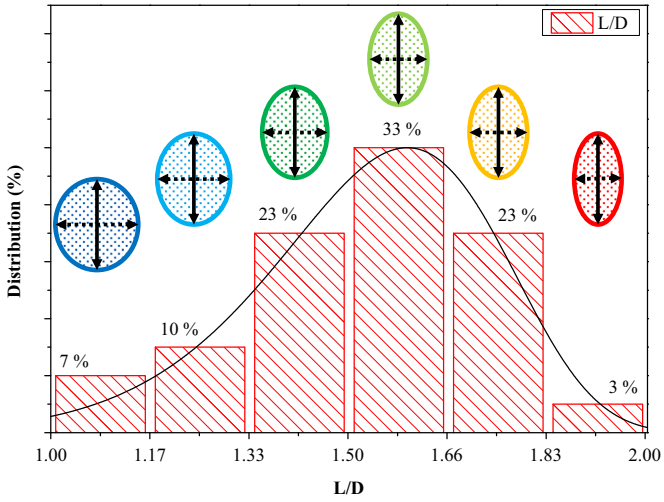


Fig. 4. *L/D* values' distribution within sample (ME-800). The obtained size distribution profile was also valid for the rest of the photocatalysts from this series (the graph was elaborated based on the measurement of 80 microeggs).

varied somewhat within 1 and 2. No clear correlations were observed between the calcination temperature and the *L/D* value. The distribution of the *L/D* value within a single sample is presented in Fig. 4, showing the dominance of the ratio interval 1.33–1.83. In the presented TEM/SEM micrographs can be also observed that the egg shaped microcrystals were "built" from polyhedral nanocrystals, which were directly evidenced by XRD.

At the applied calcination temperatures 500, 650, 800 °C, the "egg" geometry was successfully maintained, while the nanometric crystallites showed a slight increase in crystal size (confirmed also by the XRD). At 1000 °C calcination temperature, the rutilization finally occurs, as shown in Fig. 1, while at this temperature, the sintering of the individual crystallites (those which were agglomerated in egg-shapes) was inevitable, resulting randomly shaped $d > 3$ µm microcrystals (Fig. 2c). It should be mentioned here that the rutile crystals' size cannot be determined with XRD due to the inapplicability of the Scherrer equation at high crystallite size ranges (above 100 nm).

### 3.2. Structure and morphology of the single crystal anatase $TiO_2$

In the present case, the calculation of the particle size using the Scherrer equation is also pointless, because all samples' crystal size was greater-than 100 nm, which falls out from the interpretation interval of the Scherrer equation. Therefore, only the crystal phase identification was possible. In all the cases only the presence of $TiO_2$ anatase crystal phase was detected (Fig. 5), while no peaks of any impurities or other titania crystal phases were noticed.

The first aspect investigated was the influence of the hydrothermal treatment time. In the case of shorter hydrothermal treatment (1 h, sample MP-1 H) the nanoplates have rounded-off corners, meaning that only the {001} crystallographic plane family has clearly formed. It means that the

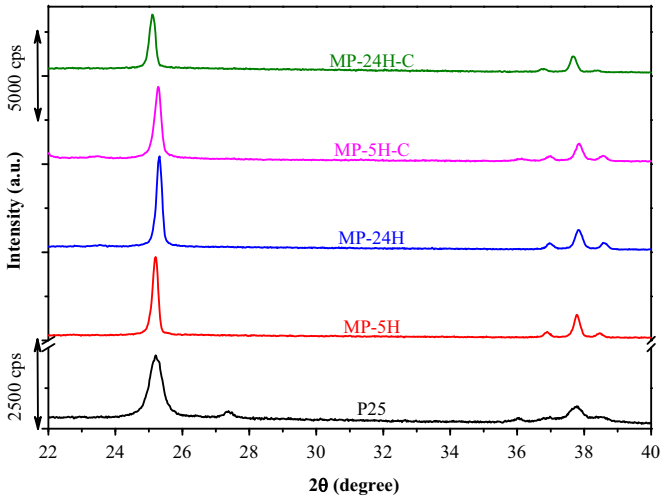


Fig. 5. XRD patterns of the MP sample series.

crystallization process is not yet completed. The sample itself was monodisperse meaning that the shape and size ( ≈ 1 μm) of all of the microparticles were in the same range. When the hydrothermal treatment time reached 5 h, the boundaries between the crystallographic planes appeared. Meanwhile, the shape and size of the particles still remained in the same interval. If the hydrothermal treatment time is longer than 24 h, the sample will be characterized by a high degree of polydispersity, while the shape of the crystals do not change. Furthermore, no significant changes were observed in the morphology and structure of the calcined MP series samples. Hence only the ones heat treated at 400 °C will be studied in the following chapters.

### 3.3. Raman spectroscopy

As a clear increase in the particle size was only observable trough the SEM micrographs, it was important to get direct evidences related to the crystallinity degree of the MP samples. Furthermore, in the case of hydrothermal crystallization procedures the possibility of some amorphous titania cannot be excluded, emphasizing the importance of this investigation. This issue was vital, because sample MP-1H and sample MP-1H-C was kept in the autoclave only for 1 h at the desired temperature (180 °C). Fig. 6 reveals the presence of the characteristic bands characteristic for $TiO_2$ anatase located at 144, 394, 512 and 635 $cm^{-1}$, respectively [54,55]. Taking into consideration that titania has a high Raman cross-section and the signal is visibly risen in intensity as the crystallinity degree of $TiO_2$ structure increases, one can infer that the extremely low intensity recorded in the case of MP-1H and MP-1H-C, in comparison with the other photocatalysts from this series, shows the existence of a relatively significant amount of amorphous material. This excludes them to be further tested for photocatalytic applications. Additionally, it should be noted here, that the ME sample series does not contain amorphous titania (that is why no separate section was dedicated to this issue).

### 3.4. Optical properties of the ME and MP sample series

Before the evaluation of the photocatalytic activities it is crucial to analyze the optical properties of these materials. If there are no significant differences in their optical peculiarities, then the comparison proposed in Section 3.3 is valid. The most appropriate methodology for this is the first derivative DRS spectrum of the individual materials [56] .The DRS spectra measured in reflectance presents the well-known adsorption edge from which the band-gap of the nanomaterials can be determined. The first derivative spectrum is even more sensitive, as any changes in the curvature in the spectrum can be visualized as individual peaks and can be associated with the possible electron-transition bands [54].

In the case of MP (Fig. 7) a single peak can be observed at 372 nm, which corresponds to the electron transition band of anatase [20,42]. This was the case of ME series also (although a slight transition of the band was noticed to 376 nm, which is insignificant in our case). As it was shown in the previous sections ME-1000 contains only rutile. This fact is also reflected in Fig. 7. For informative purposes P25 was also

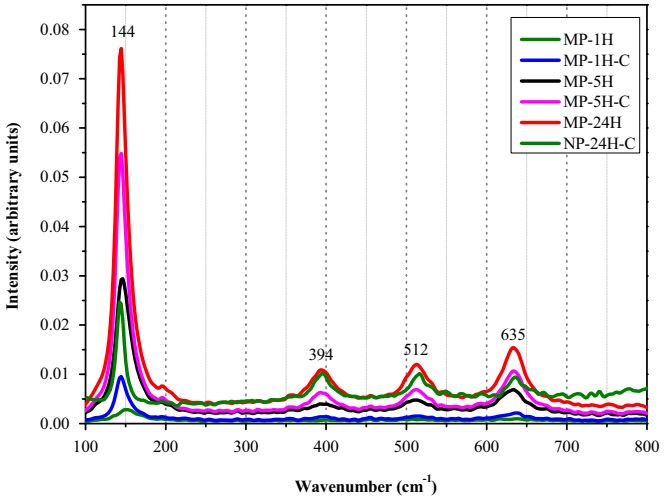


Fig. 6. Raman spectra of the MP series.

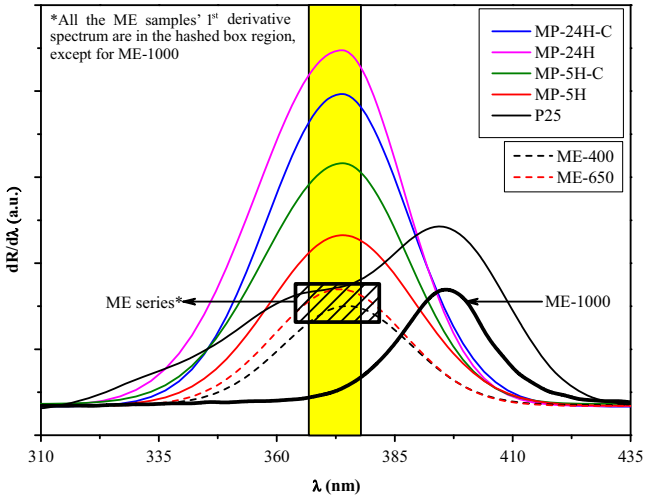


Fig. 7. First derivative DRS spectra of the ME and MP photocatalysts.

illustrated, which shows one peak at 376 nm (anatase) and one peak for rutile at 400 nm (rutile).

As there are no significant differences in the optical properties (band-gap values/ possible electron-transition bands) of the two type of titanias, the obtained photocatalytic performances can be interpreted more clearly.

### 3.5. Photocatalytic activity

The ME and MP series' photocatalytic activity was investigated for phenol degradation under UV irradiation considering multiple facts and parameters. Two approaches are considered in catalytic/photocatalytic processes: the classical one, using weight normalized kinetic parameters (e.g. reaction rates), or surface normalized kinetic approaches (e.g. surface normalized reaction rates). Both have advantages and disadvantages. For the industry, the weight normalized parameter is more convenient, because the pricing unit of a catalyst usually is defined weight dependent. Although, catalytically, the surface normalized degradation is more important, because in each case the catalytic processes are surface quality/size dependent phenomena. Accordingly, the phenol degradation rates were normalized on the surface and surface efficiency degradation curves were also plotted.

#### 3.5.1. Activity of the micro-egg-shaped $TiO_2$ anatase

The $TiO_2$ microeggs' photocatalytic activity was investigated for phenol degradation, under UV light irradiation using Aeroxide P25 (Evonik Industries) $TiO_2$ as the reference photocatalyst (Figs. 8a and 9a, b). With the increase of the calcination temperature a photocatalytic activity enhancement was observed, as it was shown in Table 1. The phenol degradation yield in the case of ME series was 39.4% (sample ME), up to 61.2% (sample ME-800). The ME-1000 sample was inactive due to the large particle size and the complete absence of the anatase phase.

In terms of initial degradation rate, P25 achieved $6.71 \cdot 10^{-3}$ mM $min^{-1}$ whilst the best performing ME sample's (ME-800) activity reached only $3.72 \cdot 10^{-3}$ mM $min^{-1}$. Although the differences between the two degradation rates are significant, the efficiency of the sample ME-800 and P25 were comparable (in degradation yield terms).

Subsequently, the surface normalized degradation intensity of phenol was determined using the procedure described at the end of Section 2.4.1, and a reversed order of activity was established within the ME series. The surface normalized degradation rates were remarkably low, varying between $0.18 \cdot 10^{-4}$ (sample ME) and $0.37 \cdot 10^{-4}$ mM $m^{-2}$ $min^{-1}$. These were much smaller values than the one calculated for P25: $1.42 \cdot 10^{-4}$ mM $m^{-2}$ $min^{-1}$. To clarify the reason behind of this phenomenon the photocatalytic activity of the single crystal/plate-shaped anatase nanocrystals' activity should be evaluated.

#### 3.5.2. Activity of the single crystal $TiO_2$ anatase – Figs. 8 b and 9a, b

As already discussed in the appropriate sections, the main method in the increase of the crystallinity grade was the

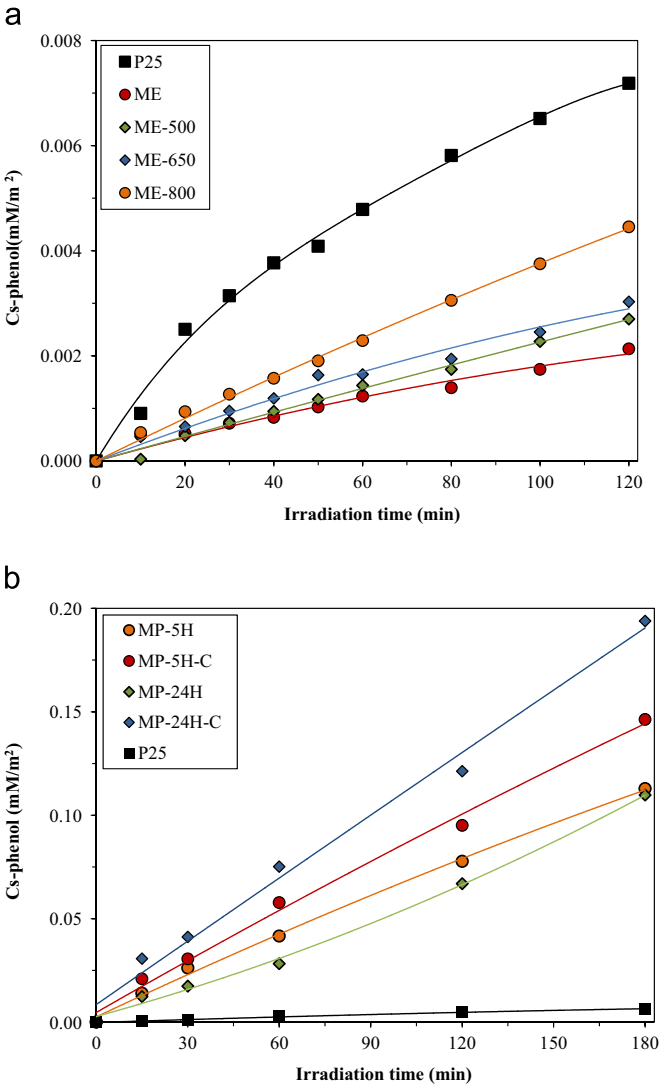


Fig. 8. Photocatalytic activity of the ME (a) and MP (b) photocatalysts for UV light driven phenol degradation.

increase of the hydrothermal treatment time and a supplementary calcination at 400 °C. It was observed that with the hydrothermal treatment time increase, and after the calcination, all samples' activity was significantly enhanced (from 5.81 to 9.65 mM $min^{-1}$ $m^{-2}$ and from 6.16 to 13.66 mM $min^{-1}$ $m^{-2}$). Furthermore, each these normalized values were superior compared to P25.

It should be noted that MP photocatalysts surface area values are very small, thus after the surface normalization, the photocatalytic activities were much higher ($13.66 \cdot 10^{-4}$ mM $min^{-1}$ $m^{-2}$) than the one shown by P25 ($0.41 \cdot 10^{-4}$ mM $min^{-1}$ $m^{-2}$).

#### 3.5.3. Shape-tailored agglomerated polycrystalline samples vs. single crystals – activity evaluation approaches

As it was detailed in the previous two sections, the activity of the photocatalysts can be examined taking in count two approaches. The first one considers that the efficiency of the photocatalyst is shown by the effective amount of pollutant degraded by a specific amount (weight) of photocatalyst. The

second approach points out that the photocatalytic processes' phenomenology is strongly related to the quality and size of the available surface. For the latter one, there are also interesting examples in the literature [57].

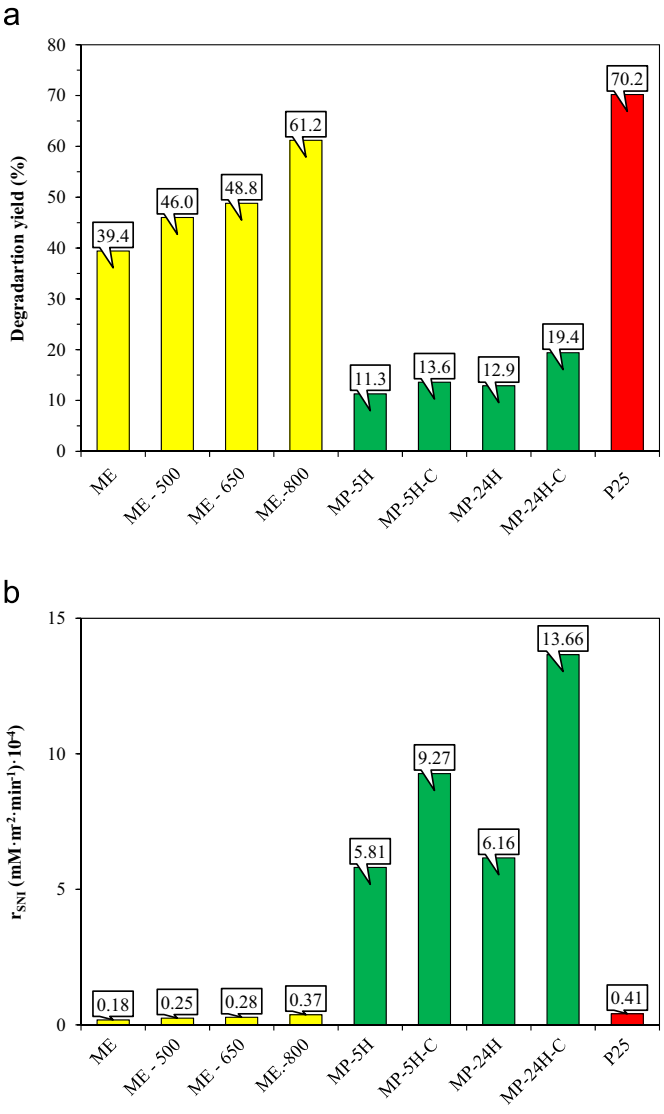


Fig. 9. (a) The comparison of the different degradation yields. (b) Normalized photocatalytic efficiencies of the studied sample series.

To examine more closely this phenomenon a "limitative approach" was considered. The lowest possible time quantum which can be considered is the lifetime of the charge carriers, which is around 10 ns [58] in anatase crystals (the authors emphasize the fact that a longer time interval can be also considered/deliberate for the calculation, although the results are more representative at the proposed time-scale). For the detailed calculation please consult Supplementary data.

The number of degraded phenol molecules ($N_{deg.\ phen.}$) was established applying the following equation ($V_{susp}$ – the volume of the applied suspension – 50 mL, $C_{deg.\ phen.}$ – the degraded phenol in terms of concentration units in mol L$^{-1}$, $t_{rec.}=10^{-8}$ s – the recombination time of the charge carriers, $N_A$ – the Avogadro number, $t_{exp}$ – the duration of the photocatalytic experiments in seconds) (Eq. (2)):

$$N_{deg.phen.} = \frac{V_{susp} \cdot C_{deg.phen.} \cdot t_{rec} \cdot N_A}{1000 \cdot t_{exp}} \quad (2)$$

The trends shown by the number of the degraded phenol molecules (Table 2) shows the same activity trend, as in the case of unnormalized activities: the most active photocatalyst was the Aeroxide P25, followed by the ME series (ME-800) and finally by the MP series. If the number of the degraded phenol molecules is estimated relatively to the surface area ($N_{deg.\ phen.surf}$), the trend changes. The new activity order resemble with the one established by the normalized concentration values.

In order to evaluate the individual efficacy of a single microparticles, the surface area (geometrical surface area – very important aspect of which importance will be revealed later on) of the average microcrystallites' was evaluated. An average particle (it should be emphasized here again that between the samples MP-5H, MP-5H C, MP-24 and MP-24H C was no significant difference in the particle size) of the MP series possessed $S_{GEO-MP}=7.2\ \mu m^2$, while in the case of ME (there were no significant differences also between the ME series members' microparticles size – the only difference was in the crystal size of the polycrystalline particles which formed the eggs) series this value was $S_{GEO-ME}=8.9\ \mu m^2$. Hence, the theoretical number of degraded phenol molecules can be estimated ($N_{deg.\ phen.\ geo.}$), which was performed by a specific number of particles ($10^8$ microparticles):

$$N_{deg.phen.geo} = 10^8 \cdot S_{GEO} \cdot N_{deg.phen.surf.} \quad (3)$$

Table 2
Short time (10 ns) degradation data of the obtained titanias.

| Sample | Crystal phase | $N_{deg.phen.} \cdot 10^6$ (no. of phenol molecules) | $N_{deg.phen.surf} \cdot 10^{-9}$ (n0. of phenol molecules μm$^{-2}$) | Surface area (m$^2$ g$^{-1}$) | $S_{GEO}$ (μm$^2$) | $N_{deg.phen.geo}$ (no. of phenol molecules degraded on $10^8$ microcrystals) |
|---|---|---|---|---|---|---|
| ME | Anatase | 8.24 | 4.5 | 91.51 | 8.9 | 4.0 |
| ME-500 | Anatase | 9.62 | 5.8 | 82.94 | | 5.2 |
| ME-650 | Anatase | 10.20 | 6.1 | 84.43 | | 5.4 |
| ME-800 | Anatase | 12.80 | 9.3 | 68.52 | | 8.3 |
| ME-1000 | Rutile | – | – | 0.22 | – | – |
| MP-5H | Anatase | 1.58 | 207.0 | 0.57 | 7.2 | 184.5 |
| MP-5H C | Anatase | 1.90 | 273.0 | 0.52 | | 243.4 |
| MP-24H | Anatase | 1.80 | 275.0 | 0.49 | | 245.0 |
| MP-24H C | Anatase | 2.70 | 451.00 | 0.45 | | 401.2 |
| P25 | ** | 14.70 | 15.0 | 49.10 | – | – |

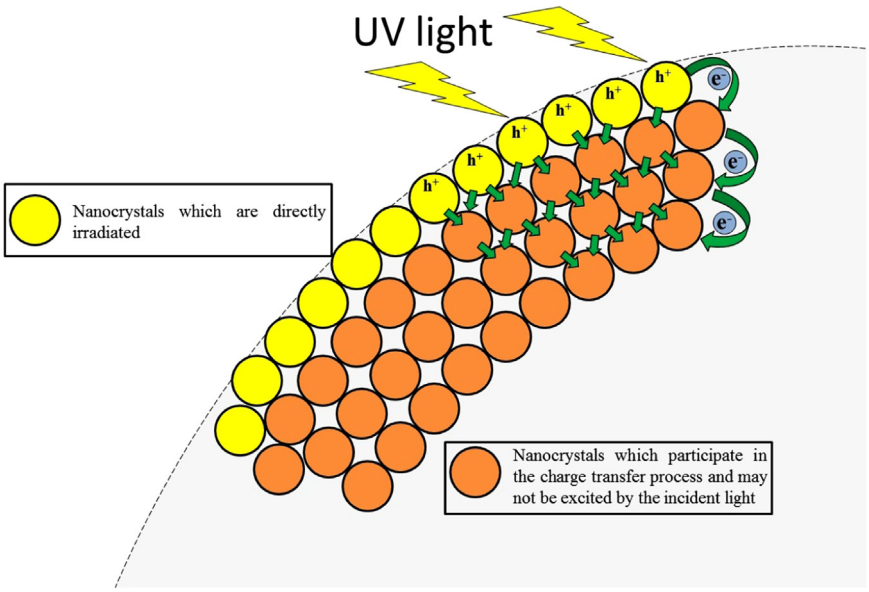


Fig. 10. Activation mechanism, and charge transfer possibilities, within the ME sample series.

The above listed equation contains: $N_{\text{deg. phen.surf.}}$ – the number of degraded phenol molecules in a 10 ns interval normalized to the surface, $S_{GEO}$ – the geometrical surface of a single microcrystal (in $\mu m^2$). The resulted number is a theoretical one which considers the fact that only the geometrical surface is accessible for the light and for the pollutants.

The obtained values showed that the single crystal anatase (MP series) should be more active compared to P25 and ME series. However, the readers are reminded, that geometrical area was used for this estimation, which is directly accessible by the light and the reaction medium (water). This means that there are further "areas" of ME sample which should be active. This supposes two possible reaction pathways (the authors do not want to "vote" for a specific scenario as no current data is available to prove the validity of "a" and "b"):

a. The surface area of the bulk polycrystalline particles are also used – reinforces, that photocatalytic reaction are also occurring at the surface of the inner particles in the eggs of the ME series.
b. The charge carriers are extremely well separated, by the inter-particle contacts and the geometrical surface shows an enhanced activity. More precisely the crystals at the surface of the egg shape are activated, while the bulk crystals act as charge carrier separators (Fig. 10).

Also it should be considered that scenario "a" and "b" can be balanced and concomitantly possible.

The results (Table 2) indicate also further shocking information. As can be seen in each case, during 10 ns, applying $10^8$ microcrystals, only max. 401 phenol molecules can be degraded, which is extremely low (within 10 ns), emphasizing that photocatalysis has a lot of work in the near future to improve these numbers.

## 4. Conclusions

As several synthesis strategies are currently available in the literature regarding the shape-tailored titanias, including different organization levels for shape tailoring (hierarchical build-up vs. single crystal shape tuning) higher activities are desired. In the present work it was shown that both strategies are feasible paths to obtain high activity photocatalysts. Each of the approaches presented a specific advantage, such as efficient crystal planes (single, exposed faceted anatase crystals) or efficient charge separation/inner particle activation (polycrystalline particle coupling within the hierarchical organization). However, it was pointed out that in each case the potential of the photocatalysts are not exploited (it can be said that the current level is the minimum) at all and further hard work is needed.

## Acknowledgments

The authors from Hungary would like to express their gratitude to the Grant from Swiss Contribution (SH/7/2/20). The authors from Romania would like to thank to the Romanian National Authority for Scientific Research, CNCS – UEFISCDI, project number PN-II-ID-PCE-2011-3-0442 for the financial support. Furthermore, all the authors would like to thank to the Romanian-Hungarian bilateral project nr. 661/2013/K-TÉT_12_RO-1-2013-0109966.

## Appendix A. Supplementary material

Supplementary data associated with this article can be found in the online version at http://dx.doi.org/10.1016/j.ceramint.2015.10.095.

## References


[1] L.M. Pastrana-Martínez, S. Morales-Torres, V. Likodimos, J.L. Figueiredo, J.L. Faria, P. Falaras, A.M.T. Silva, Advanced nanostructured photocatalysts based on reduced graphene oxide–$TiO_2$ composites for degradation of diphenhydramine pharmaceutical and methyl orange dye, Appl. Catal. B Environ. 123 (2012) 241–256.

[2] J. Virkutyte, V. Jegatheesan, R.S. Varma, Visible light activated $TiO_2$/microcrystalline cellulose nanocatalyst to destroy organic contaminants in water, Bioresour. Technol. 113 (2012) 288–293.

[3] N.S. Andryushina, O.L. Stroyuk, Influence of colloidal graphene oxide on photocatalytic activity of nanocrystalline $TiO_2$ in gas-phase ethanol and benzene oxidation, Appl. Catal. B Environ 148–149 (2014) 543–549.

[4] Y. Liu, H. Wang, H. Li, W. Zhao, C. Liang, H. Huang, Y. Deng, H. Shen, Length-controlled synthesis of oriented single-crystal rutile $TiO_2$ nanowire arrays, J. Colloid. Interface Sci. 363 (2011) 504–510.

[5] Y.-K. Yuan, X.-L. Xiao, Y.-S. Wang, J.-H. Xue, G.-R. Li, R.-H. Kang, J.-Q. Zhang, L.-F. Shi, Quartz crystal microbalance with-cyclodextrin/$TiO_2$ composite films coupled with chemometrics for the simultaneous determination of urinary 1- and 2-naphthol, Sens. Actuators B 145 (2010) 348–354.

[6] P.-G. Su, L.-N. Huang, Humidity sensors based on $TiO_2$ nanoparticles/polypyrrole composite thin films, Sens. Actuators B 123 (2007) 501–507.

[7] Z. Wu, W. Zhang, F. Xiong, Q. Yuan, Y. Jin, J. Yang, W. Huang, Active hydrogen species on $TiO_2$ for photocatalytic $H_2$ production, Phys. Chem. Chem. Phys. 16 (2014) 7051–7057.

[8] Y.J. Zhang, W. Yan, Y.P. Wu, Z.H. Wang, Synthesis of $TiO_2$ nanotubes coupled with CdS nanoparticles and production of hydrogen by photocatalytic water decomposition, Mater. Lett. 62 (2008) 3846–3848.

[9] R.J. Tayade, R.G. Kulkarni, R.V. Jasra, Transition Metal Ion, Impregnated mesoporous $TiO_2$ for photocatalytic degradation of organic contaminants in water, Ind. Eng. Chem. Res. 45 (2006) 5231–5238.

[10] S.K. Kavitha, P.N. Palanisamy, Photocatalytic degradation of vat yellow 4 using UV/$TiO_2$, Modern Appl. Sci. 4 (2010) 125–130.

[11] J. Virkutyte, V. Jegatheesan, R.S. Varma, Visible light activated $TiO_2$/microcrystalline cellulose nanocatalyst to destroy organic contaminants in water, Bioresour. Technol. 113 (2012) 288–293.

[12] H. Zhang, P. Zhang, Y. Ji, J. Tian, Z. Du, Photocatalytic degradation of four non-steroidal anti-inflammatory drugs in water under visible light by P25-$TiO_2$/tetraethyl orthosilicate film and determination via ultraperformance liquid chromatography electrospray tandem mass spectrometry, Chem. Eng. J. 262 (2015) 1108–1115.

[13] R.J. Tayade, P.K. Surolia, R.G. Kulkarni, R.V. Jasra, Photocatalytic degradation of dyes and organic contaminants in water using nanocrystalline anatase and rutile $TiO_2$, Sci. Technol. Adv. Mater. 8 (2007) 455–462.

[14] D.A.H. Hanaor, C.C. Sorrell, Review of the anatase to rutile phase transformation, J. Mater. Chem. 46 (2011) 855–874.

[15] H.G. Yang, C.H. Sun, S.Z. Qiao, J. Zou, G. Liu, S.C. Smith, H.M. Cheng, G.Q. Lu, Anatase $TiO_2$ single crystals with a large percentage of reactive facets, Nature 453 (2008) 638–641.

[16] F. Labat, P. Baranek, C. Domain, C. Minot, C. Adamo, Density functional theory analysis of the structural and electronic properties of $TiO_2$ rutile and anatase polytypes performances of different exchange-correlation functionals, J. Chem. Phys. 126 (2007) 154703–154714.

[17] J.K. Dong, H.H. Sung, H.O. Sung, J.K. Eui, Influence of calcination temperature on structural and optical properties of $TiO_2$ thin films prepared by sol–gel dip coating, Mater. Lett. 57 (2002) 355–360.

[18] W. Li, C. Ni, H. Lin, C.P. Huang, S.I. Shah, Size dependence of thermal stability of $TiO_2$ nanoparticles, J. Appl. Phys. 96 (2204) 6663–6670.

[19] M.J. Sampaio, C.G. Silva, R.R.N. Marques, A.M.T. Silva, J.L. Faria, Carbon nanotube–$TiO_2$ thin films for photocatalytic applications, Catal. Today 161 (2011) 91–96.

[20] L. Baia, A. Vulpoi, T. Radu, É. Karácsonyi, A. Dombi, K. Hernádi, V. Danciu, S. Simon, K. Norén, S.E. Canton, G. Kovács, Zs. Pap, $TiO_2$/$WO_3$/Au nanoarchitectures' photocatalytic activity "from degradation intermediates to catalysts' structural peculiarities" part II: aerogel based composites – fine details by spectroscopic means, Appl. Catal. B Environ. 148–149 (2014) 589–600.

[21] M. Murdoch, G.I.N. Waterhouse, M.A. Nadeem, J.B. Metson, M.A. Keane, R.F. Howe, J. Llorca, H. Idriss, The effect of gold loading and particle size on photocatalytic hydrogen production from ethanol over Au/$TiO_2$ nanoparticles, Nat. Chem. 3 (2011) 489–492.

[22] K. Vajda, K. Mogyorósi, Z. Németh, K. Hernádi, L. Forró, A. Magrez, A. Dombi, Photocatalytic activity of $TiO_2$/SWCNT and $TiO_2$/MWCNT nanocomposites with different carbon nanotube content, Phys. Status Solidi B 248 (2011) 2496–2499.

[23] É. Karácsonyi, L. Baia, A. Dombi, V. Danciu, K. Mogyorósi, L.C. Pop, G. Kovács, V. Coşoveanu, A. Vulpoi, S. Simon, Zs. Pap, The photocatalytic activity of $TiO_2$/$WO_3$/noble metal (Au or Pt) nanoarchitectures obtained by selective photodeposition, Catal. Today 208 (2013) 19–27.

[24] Y. Yao, G. Li, S. Ciston, R.M. Lueptow, K.A. Gray, Photoreactive Ti.O.2/Carbon Nanotube, Composites: Synthesis and Reactivity, Environ. Sci. Technol. 42 (2008) 4952–4957.

[25] B. Neppolian, A. Bruno, C.L. Bianchi, M. Ashokkumar, Graphene oxide based Pt–$TiO_2$ photocatalyst: Ultrasound assisted synthesis, Characterization and catalytic efficiency, Ultrason. Sonochem. 19 (2012) 9–15.

[26] H. Pang, Y. Li, L. Guan, Q. Lu, F. Gao, $TiO_2$/Ni nanocomposites: Biocompatible and recyclable magnetic photocatalysts, Catal. Commun. 12 (2011) 611–615.

[27] G. Yang, Z. Yan, T. Xiao, Preparation and characterization of $SnO_2$/ZnO/$TiO_2$ composite semiconductor with enhanced photocatalytic activity, Appl. Surf. Sci. 258 (2012) 8704–8712.

[28] X. Shao, W. Lu, R. Zhang, F. Pan, Enhanced photocatalytic activity of $TiO_2$-C hybrid aerogels for methylene blue degradation, Sci. Rep. 3 (2013) Art. Nr. 3018.

[29] M. Xinchun, W. Zhiqiang, L. Xiufeng, H. Qunqing, W. Bo, D. Dongxu, Z. Chuanyao, L. Li-Min, Y. Xueming, Effect of Surface Structure on the Photoreactivity of $TiO_2$, J. Phys. Chem. C 119 (2015) 6121–6127.

[30] X. Quanlong, Y. Jiaguo, Z. Jun, Z. Jinfeng, L. Gang, Cubic anatase $TiO_2$ nanocrystals with enhanced photocatalytic $CO_2$ reduction activity, Chem. Commun. 51 (2015) 7950–7953.

[31] Y. Zhang, Y. Jin, X. Huang, H. Shi, G. Zhao, H. Zhao, Nanocrystalline {001} $TiO_2$/carbon aerogel electrode with high surface area and enhanced photoelectrocatalytic oxidation capacity, Electrochim. Acta 130 (2014) 194–199.

[32] X. Juan, T. Fei, X. Chuangye, Y. Yang, Y. Liming, K. Yandong, Unique anatase $TiO_2$ twinning crystals formed by high energy{001} facets and the improved photocatalytic activity, J. Phys. Chem. C 119 (2015) 13011–13020.

[33] S. Jian-Wen, X. Chong, H. Chi, L. Chang, G. Chen, Y. Shenghui, C. Jian-Wei, L. Guodong, Photocatalytic performance comparison of titania hollow spheres composed of nanoplates with dominant {001} facets and nanoparticles without dominant {001} facets, Catal. Commun. 66 (2015) 46–49.

[34] E.-H. Kong, J. Lim, J.H. Lee, W. Choi, H.M. Jang, Enhanced photocatalytic activity of {101}-oriented bipyramidal $TiO_2$ agglomerates through interparticle charge transfer, Appl. Catal. B: Environ 176 (2015) 76–82.

[35] X. Yuan, B. Gao, J. Sh, Y. Chen, B. Lin, Z. Gu, Morphologically-tunable anatase $TiO_2$ with exposed (001) facet and related photocatalytic performance, Mater. Lett. 128 (2014) 167–169.

[36] H.G. Yang, G. Liu, S.Z. Qiao, C.H. Sun, Y.G. Jin, S.C. Smith, J. Zou, H. M. Cheng, G.Q. Lu, Solvothermal synthesis and photoreactivity of anatase $TiO_2$ nanosheets with dominant {001} facets, J. Am. Chem. Soc. 131 (2009) 4078–4083.

[37] H.G. Yang, C.H. Sun, S.Z. Qiao, J. Zou, G. Liu, S.C. Smith, H.M. Cheng, G.Q. Lu, Anatase $TiO_2$ single crystals with a large percentage of reactive facets, Nature 453 (2008) 638–641.

[38] J. Chen, H. Zhang, P. Liu, Y. Wang, X. Liu, G. Li, T. An, H. Zhao, Vapor-phase hydrothermal synthesis of rutile $TiO_2$ nanostructured film with exposed pyramid-shaped (111) surface and superiorly photoelectrocatalytic performance, J. Colloid. Interface Sci 429 (2014) 53–61.

[39] H. Bai, Z. Liu, S.S. Lee, D.D. Sun, The effect of fabrication method of hierarchical 3D $TiO_2$ nanorod spheres on photocatalytic pollutants degradation, Appl. Catal. A Gen. 447–448 (2012) 193–199.

[40] B.D. Yao, Y.F. Chan, X.Y. Zhang, W.F. Zhang, Z.Y. Yang, N. Wang, Formation mechanism of $TiO_2$ nanotubes, Appl. Phys. Lett. 82 (2003) 281–283.
[41] R. Yoshida, Y. Suzuki, S. Yoshikawa, Syntheses of $TiO_2$ (B) nanowires and $TiO_2$ anatase nanowires by hydrothermal and post-heat treatments, J. Solid State Chem. 178 (2005) 2179–2185.
[42] G. Mogilevsky, Q. Chen, A. Kleinhammes, Y. Wu, The structure of multilayered titania nanotubes based on delaminated anatase, Chem. Phys. Lett. 460 (2008) 517–520.
[43] K. Vajda, Zs. Kása, A. Dombi, Z. Németh, G. Kovács, V. Danciu, T. Radu, C. Ghica, L. Baia, K. Hernádi, Zs. Pap, "Crystallographic" holes: new insights for a beneficial structural feature for photocatalytic applications, Nanoscale 7 (2015) 5776–5786.
[44] Y.S. Sohn, Y.R. Smith, M. Misra, V. Subramanian, Electrochemically assisted photocatalytic degradation of methyl orange using anodized titanium dioxide nanotubes, Appl. Catal. B 84 (2008) 372–378.
[45] R.P. Antony, T. Mathews, A. Dasgupta, S. Dash, A.K. Tyagi, B. Raj, Rapid breakdown anodization technique for the synthesis of high aspect ratio and high surface area anatase $TiO_2$ nanotube powders, J. Solid. State. Chem. 184 (2011) 624–632.
[46] D. Eder, A.H. Windle, Morphology control of CNT-$TiO_2$ hybrid materials and rutile nanotubes, J. Mater. Chem. 18 (2008) 2036–2043.
[47] D. Eder, M.S. Motta, I.A. Kinloch, A.H. Windle, Anatase nanotubes as support for platinum nanocrystals, Physica E 37 (2007) 245–249.
[48] D. Eder, I.A. Kinloch, A.H. Windle, Pure rutile nanotubes, Chem. Commun. 13 (2006) 1448–1450.
[49] J. Lin, Y. Lin, P. Liu, M.J. Meziani, L.F. Allard, Y.-P. Sun, Hot-Fluid Annealing for Crystalline Titanium Dioxide Nanoparticles in Stable Suspension, J. Am. Chem. Soc. 124 (2002) 11514–11518.
[50] G. Kovács, L. Baia, A. Vulpoi, T. Radu, É. Karácsonyi, A. Dombi, K. Hernádi, V. Danciu, S. Simon, Zs. Pap, $TiO_2$/$WO_3$/Au nanoarchitectures' photocatalytic activity, from degradation intermediates to catalysts' structural peculiarities, Part I: Aeroxide P25 based composites, Appl. Catal. B-Environ. 147 (2014) 508–517.
[51] Zs. Pap, V. Danciu, Zs. Cegléd, Á. Kukovecz, A. Oszkó, A. Dombi, K. Mogyorósi, The influence of rapid heat treatment in still air on the photocatalytic activity of titania photocatalysts for phenol and monuron degradation, Appl. Catal. B Environ. 101 (2011) 461–470.
[52] L. Castro, M.R. Nunes, A.P. Carvalho, F.M. Costa, M.H. Florêncio, Synthesis of anatase $TiO_2$ nanoparticles with high temperature stability and photocatalytic activity, Solid State Sci. 10 (2008) 602–606.
[53] G. López-Granada, J.D.O. Barceinas-Sánchez, R. López, R. Gómez, High temperature stability of anatase in titania–alumina semiconductors with enhanced photodegradation of 2, 4-dichlorophenoxyacetic acid, J. Hazard. Mater. 263 (2013) 84–92.
[54] D. Georgescu, L. Baia, O. Ersen, M. Baia, S. Simon, Experimental assessment of the phonon confinement in $TiO_2$ anatase nanocrystallites by Raman spectroscopy, J. Raman Spectrosc. 43 (2012) 876–883.
[55] L. Baia, A. Peter, V. Cosoveanu, E. Indrea, M. Baia, J. Popp, V. Danciu, Synthesis and nanostructural characterization of $TiO_2$ aerogels for photovoltaic devices, Thin Solid Films 511–512 (2006) 512–516.
[56] D. Flak, A. Braun, B.S. Mun, J.B. Park, M. Parlinska-Wojtan, T. Graule, M. Rekas, Spectroscopic assessment of the role of hydrogen on surface defects, on the electronic structure and transport properties of $TiO_2$, ZnO and $SnO_2$ nanoparticles, Phys. Chem. Chem. Phys. 15 (2013) 1417–1430.
[57] S.P. Phivilay, A.A. Puretzky, K. Domen, I.E. Wachs, Nature of Catalytic Active Sites Present on the Surface of Advanced Bulk Tantalum Mixed Oxide Photocatalysts, ACS Catal. 3 (2013) 2920–2929.
[58] N. Serpone, D. Lawless, R. Khairutdinov, E. Pelizzetti, Size effects on the photophysical properties of colloidal anatase $TiO_2$ particles: size quantization versus direct transitions in this indirect semiconductor?, J. Phys. Chem. 99 (1995) 16655–16661.